

NATURE OF TRANSONIC COMPRESSOR FLOW AND ITS 3D DESIGN IMPLICATIONS

Demetrios Lefas
Whittle Laboratory
University of Cambridge, UK
Email: dl467@cam.ac.uk

ABSTRACT

A key problem in transonic compressor and fan design is that although a 3D description of the flow is necessary to correctly capture the shock; accounting for it during the sectional design is difficult because the key driving design parameters are unknown. In this paper, it is shown that for inlet relative Mach numbers between 0.85 to 1.10, the pressure rise across the shock is a function of the 3D streamtube area at the throat A_t over the inlet area A_1 . This key finding is based on three key transonic flow features, discussed in detail within this paper, being present together across a wide range of 10,000 representative transonic compressor and fan designs published online: (<https://whittle.digital/transonic>).

This unique wide-ranging web interactive dataset reveals that the effect of changes in the blade geometry, or the 3D streamtube height, on the transonic flow field is one of the same and can be explained simply by keeping track of the associated changes in A_t/A_1 . Surprisingly, the pre-shock Mach number at a given A_t/A_1 is shown to be insensitive to the details of the blade surface geometry. Only geometric design choices made in the preliminary design phase, such as the maximum thickness and the inlet relative flow angles, are shown to have a second-order effect. These findings suggest, that the purpose of the sectional design phase should be solely to make the desired changes in the real spanwise 3D A_t/A_1 .

The second half of the paper concerns itself with the level of fidelity necessary when calculating the spanwise 3D A_t/A_1 , for it to positively influence design; especially while approaching a Mach number of unity when small changes in A_t/A_1 become increasingly important. A key conclusion is that not resolving the subtle changes in the 3D radial flow within the blade passage at the appropriate level of fidelity, especially at the early throughflow multistage compressor design stage, could potentially mislead the transonic design process. As a result, for the rapid exploration of future compressor designs, this paper advocates utilising the database of more than 10,000 transonic designs to generate an initial 3D blade, which is then assessed early in the design process using A_t/A_1 extracted from 3D CFD.

1. INTRODUCTION

Over the last several decades, a lot of research has focused on fundamentally understanding the key driving design parameters of transonic compressors and fans. In the initial stages of transonic compressor design, NACA Langley [1] and subsequently DLR [2] [3] followed an approach involving extensive testing of transonic compressor cascade tests. This involved exploring different families of blade section designs, whilst sweeping through inlet relative Mach numbers and key geometric parameters, such as maximum thickness-to-chord and pitch-to-chord ratios. These experimental campaigns clearly showed that the crucial change in performance occurred when the shock was strong enough to separate the boundary layer. However, whilst the focus was on analysing the resulting transonic flow fields to gain comprehensive insights, they did not provide much clarity on what universal parameters control a shock's strength.

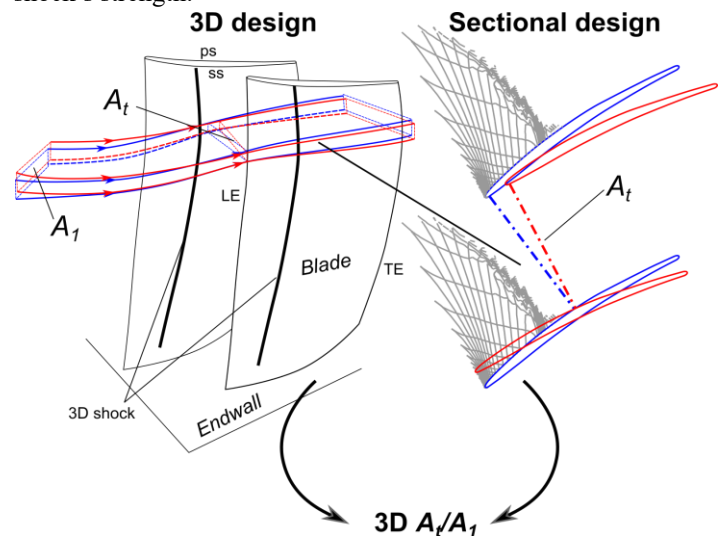


Fig. 1: Illustration of the inherent difficulty to account for 3D radial streamtube height changes when performing the design of transonic sections; simplified by accounting for the real changes in 3D A_t/A_1 .

These efforts to understand the key transonic design parameters were further complicated by the realisation that transonic compressor flows are inherently three-dimensional (3D) [4]; thus demonstrating that these early cascade (2D) tests were not really representative of the environment experienced by transonic compressors and fan sections. The key omission being, as demonstrated by the left-hand rotor schematic in Fig. 1, subtle changes in the streamtube contraction in the radial direction, as the flow progresses from a blade's leading to trailing edge during a blade's sectional design. This radial contraction becomes increasingly important approaching an inlet Mach number of unity, where for a blade thickness and have no boundary layer. The realisation of the importance of 3D flows coincided with the advent of 3D CFD, and therefore most of the investigations on transonic compressors both in academia and industry moved to this 3D computational and less so experimental environment.

A number of academic papers, primarily by industry experts, then showed the sensitivity of the 3D flow field in the transonic regime to certain geometric area ratios, like the area ratio between the passage throat and the inlet [5] [6] [7]. This area ratio parameter was primarily used as an independent variable because of its well-known association with the choking capacity of blade rows, showing also a dependence on the resulting shock structure, albeit the lack of clarity in explaining this. An attempt to clarify this for supersonic compressor blades was made by Freeman and Cumpsty [8], but only under the assumption the blades were two-dimensional (2D), thin, and had no camber up to the throat. These assumptions are not always representative, especially for blade sections operating over the transonic regime.

In summary, whilst these studies have indicated a strong sensitivity of the flow to geometric sectional area ratios in the real 3D flow environment, there is a clear gap in our understanding of how subtle changes in the 3D radial streamtubes shown in Fig. 1, that naturally occur during the design process, affect the resulting shock structure. For example, the right-hand side of Fig. 1 shows how altering the local stagger of a section (from blue to red) increases the geometric throat area width (A_t). However, this change also impacts the streamtube enclosing the section in two ways: 1) by shifting its inlet radius and altering the inlet area (A_i), and 2) by adjusting the radial streamtube height within the blade passage, thus affecting the throat area height (A_t). Hence, the difficulty in accounting for these subtle, but important at transonic speeds, streamtube changes during the sectional design. This explains why recent 3D transonic design papers focus on methods that do not require physical intuition, such as multi-objective inverse, adjoint and machine learning optimisation schemes in 3D CFD [9], [10] & [11].

More recently, the author showed and explained [12] [13] the dependence of the shock on 3D A_t/A_i in the transonic regime, which for simplicity is referred to as A_t/A_i from here on. This parameter can be visualized more simply by considering a blade-to-blade view together with a meridional view of the radial streamtube using Fig. 2. It is defined in the blade-to-blade view as the geometric throat area o , over the inlet area A_i , times in the

meridional view the radial streamtube height change up to the throat plane A_{xt}/A_{x1} . More specifically, it was shown that the resulting spanwise A_t/A_i distribution is dominated by 3D radial spanwise contraction changes A_{xt}/A_{x1} , which need to be taken into account in the design of transonic rotors.

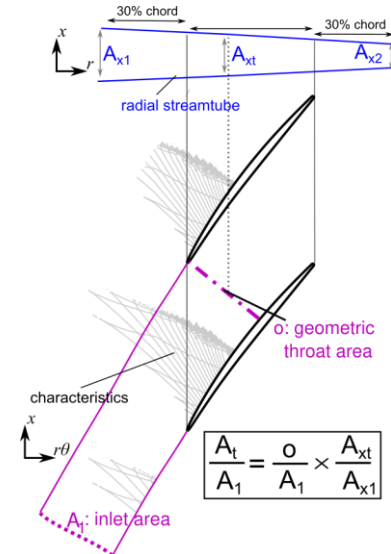


Fig. 2: Quasi-3D view of a transonic compressor blade section, with the important area ratio of A_t/A_i , also shown.

This paper aims to take a step further and comprehensively show for the first time what the key flow physics are, and what ultimately controls a blade's shock strength in the transonic regime, based on a large interactive dataset of more than 10,000 quasi-3D representative transonic blade designs. The database is provided in a web-based visualisation powered by dbslice¹ [14] [15]. The purpose of the dataset is to analyse and discuss in detail in this paper only one representative design example of a blade section operating at an inlet relative Mach number of 0.95, whilst giving the reader the freedom to apply the same key findings to the broader design space covered by civil compressors and fans, and convince themselves of their wide universality.

In the first half of the paper, it will be shown that over most of a civil transonic compressor and fan's operation, 3D A_t/A_i primarily sets the final shock structure because of three key flow features being present. Whilst treating blade section design as a 2D problem approaching a Mach number of unity is incorrect, what this paper will demonstrate is that tracking spanwise 3D A_t/A_i changes during the sectional design, is the key to understanding the resulting changes in the transonic flow field. Hence, by accurately calculating A_t/A_i in a representative 3D CFD environment, both the changes in the geometry and the subtle changes in the 3D radial streamtube contraction can be simply considered simultaneously; as illustrated in Fig. 1.

The second half of the paper discusses the implications of this newfound clarity to practical design; particularly the early design phase usually based on lower-order streamline curvature throughflow methods. It aims to answer three key questions:

- 1) What are the key geometric and aerodynamic preliminary sectional design parameters?

¹ <https://whittle.digital/transonic>

- 2) What level of fidelity is necessary when calculating the 3D A_1/A_1 for it to positively influence design?
- 3) How can the early design phase be improved using the database of 10,000 A_1/A_1 blades generated in this paper?

2. METHODOLOGY

This section provides an overview of the design methodology adopted for the definition of each transonic compressor blade section presented in this paper's wide transonic compressor dataset, and goes over the numerical solvers used to analyse the transonic flow field. Three levels of numerical fidelity were used as part of this paper: 1) a quasi-3D solver, 2) a throughflow/streamline curvature solver and 3) a 3D CFD solver.

2.1 Design Methodology

A typical transonic compressor blade section design is shown in Fig. 3(a), which is defined by a camber line shown in red, whose direction is given by χ , and a symmetric thickness distribution, which is added on either side of the camber line to define the blade's suction and pressure surfaces. In addition, to account for the real 3D radial contraction effects in this study, a streamtube contraction is applied across the blade linearly from 30% chord upstream of the leading edge to 30% chord downstream of the trailing edge, as shown in Fig. 2. The choice of a linear radial contraction distribution is made for simplicity.

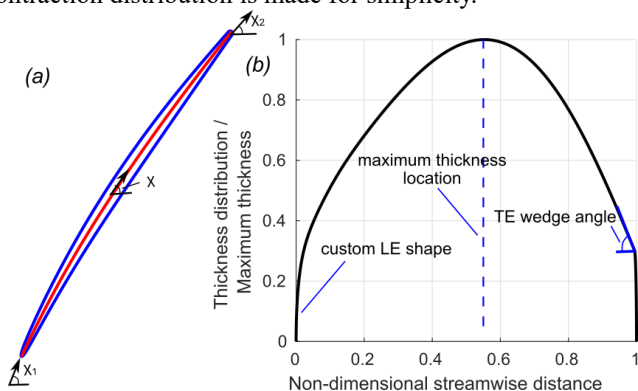


Fig. 3: (a) Schematic of typical compressor blade design defined from a camber (in red) and symmetric thickness distribution & (b) definition of thickness distribution.

The thickness distribution, non-dimensionalised by maximum thickness, is shown in Fig. 3(b). It has been defined using the shape space method proposed by Kulfan [16] and used previously successfully by Goodhand et al. [17] to define transonic elliptical leading edges. Using the shape space method of Kulfan, the leading edge shape, radius, maximum thickness location, trailing edge wedge angle and overall thickness distribution shape can be independently set, whilst ensuring curvature continuity. These shape space thickness parameters have been prescribed to be representative of modern transonic compressor blades and are fixed throughout this paper. When changing the key geometric variable of maximum thickness later in the paper, this whole thickness distribution is scaled whilst maintaining its shape. Finally, a circular trailing edge is applied.

Fig. 4 shows the camber distributions, defined by $(\chi - \chi_1)/(\chi_1 - \chi_2)$. A linear distribution is applied up to the point termed 'joint'

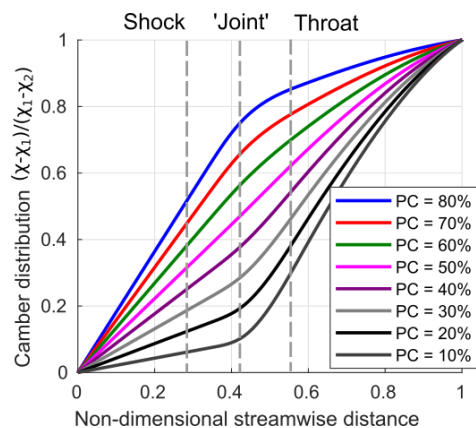


Fig. 4: Definition of camber distribution for transonic profiles.

in the figure, and a cubic from there onwards. The cubic distribution has a reducing gradient towards the trailing edge, such as to minimise the amount of subsonic turning done where the boundary layer shape factor is higher.

The position at which the shock terminates, shown in Fig. 4 by the left-most grey dashed line for a given design case, is always designed to lie within the linear region. Given that the radial streamtube contraction applied is linear, selecting a linear distribution for the camber distribution up to the shock ensures a smooth continuous supersonic acceleration up to the shock foot, which is aerodynamically desirable. A different distribution could be chosen, which could also result in a smooth acceleration but as will be shown later in Section 5, this is of second-order importance compared to the absolute value of A_1/A_1 .

In order to study the effect of A_1/A_1 , whilst varying key aerodynamic and geometric parameters, the distribution of camber up to the 'joint' is kept linear whilst the percentage camber, PC , up to that point is changed. The location of the 'joint' in Fig. 4 is set at the midpoint between the plane where the shock terminates and the throat plane. The throat plane is defined as the minimum cross-sectional area within the blade passage, when calculated normal to the mid-passage streamline, including the displacement from the boundary layer. The location of the 'joint' in Fig. 4 is not a fixed geometric point during the design as the shock and throat location, and by extension the 'joint' location, will vary. In Fig. 4 the 'joint' location is kept fixed to show the effect of changing PC on the camber distribution.

This choice of 'joint' location is justified because it results in close to the optimum operating incidence range; an observation not analysed here for conciseness, but being based on a wide range of transonic blade designs. The underlying reason is that if the 'joint' was placed at the shock position, then at negative incidence, as the shock moves towards the throat plane it will accelerate and terminate in a high camber region. On the other hand, if the 'joint' was placed at the throat position, then there would be unnecessarily too much camber required in the subsonic diffusion post-shock part of the blade.

Finally, the inlet χ_1 and outlet χ_2 blade metal angles are defined based on the desired target inlet and outlet Mach number triangles. The inlet blade metal angle χ_1 is defined such that the local incidence onto the blade is zero. The outlet blade angle χ_2 is changed until the target outlet relative flow angle is met.

In summary, the blade design methodology adopted in this paper aims to allow for the study of a wide range of transonic blade designs, whilst varying the key geometric and aerodynamic design parameters. Defining the camber and thickness distribution in the systematic representative way described in this section, allows for a holistic study of the important transonic compressor flow physics whilst considering only good aerodynamic designs; thus minimising the size of the transonic compressor dataset needed.

The design space generated covers a wide range of key geometric and aerodynamic design parameters listed in Table 1, which include most of the design space of civil transonic compressors and fans. Whilst only specific examples from this database will be highlighted in the rest of this paper, the web-interactive database published online allows the readers to explore the data on their own and check the validity of the ideas presented hereon. More information on the web interactive database, and how it can be used to sort through subsets of the design space are provided in Section 8.

Inlet relative Mach number, M_{1rel} :	0.85 – 1.10
Inlet relative flow angle, α_{1rel} :	45° – 65°
Loading coefficient, ψ :	0.30-0.45
Total radial contraction, A_{x2}/A_{x1} :	0.85-1.0
Thickness-to-chord, t/c :	2-5%
Pitch-to-chord, s/c :	0.70-1.0
Percentage camber up to the throat, PC	-10%-80%

Table 1: Summary of the range of key geometric and aerodynamic parameters covered by the design space generated.

2.2 Numerical Methodology

The MISES [18] quasi-3D inviscid/viscous solver CFD code was employed in all quasi-three-dimensional designs studied. MISES solves the inviscid steady Euler equations on a two-dimensional H-grid with a coupled integral compressible boundary layer solver. The grid dynamically adapts to the solution ensuring that the mesh elements lie on streamlines. In addition, the displacement thickness of the boundary layer predicted from the coupled boundary layer solver is used as the first grid point adjacent to the blade surface.

The turbulence intensity was specified in the code as typically found in compressors ($Tu=4\%$) and was run at a Reynolds number of one million. Boundary layer transition was enforced right at the leading edge of both the pressure and suction surface by enforcing the turbulent closure relations in the compressible boundary layer solver [19].

The MISES CFD code has been chosen for two reasons. First, as it is quick and has been extensively calibrated against experiments, showing an excellent correlation to pressure and loss profiles of transonic airfoils [19] and transonic compressor cascades [20] [21]. Second, because the solver is quasi-3D.

The use of quasi-3D CFD is key because it allows the radial streamtube contraction across the blade row, shown in blue in Fig.

2, to be a free variable and to be varied independently. In other words, by using this approach the effect of changing the geometry of the section can be decoupled from the accompanying changes in the streamtube enclosing that section and vice versa. This approach allows the quick, but also accurate, assessment of the relative importance of the real 3D flow environment on the resulting shock structure.

Whilst the MISES CFD code makes possible such a wide-ranging study of transonic quasi-3D designs, leading to an improved understanding of the fundamental physics driving a shock's behaviour, it fails to consider how alterations in a 3D rotor's sectional geometry affect the corresponding 3D radial flow within the blade passage; as depicted in Fig. 1. Hence to properly study this important effect, the 3D CFD solver TURBOSTREAM is used [22]. TURBOSTREAM is a structured multi-block Reynolds-averaged Navier–Stokes (RANS) solver based upon Denton's TBLOCK and implemented for parallel GPU operation. The turbulence model used is the Spalart-Allmaras [23].

The streamline curvature throughflow program SLEQ used in Section 7 to compare with the 3D CFD has been developed by Denton [24]. More details on the setup for the throughflow calculation will be provided in Section 7.

3. KEY TRANSONIC COMPRESSOR FLOW PHYSICS

There are three flow features specific to transonic compressors that result in A_t/A_1 primarily setting its shock structure. These are:

- A. the shock terminates ahead of the throat plane,
- B. the static pressure is relatively uniform by the throat plane &
- C. an effectively isentropic streamtube exists within the blade passage.

This part of the paper explains in detail the validity of these assumptions for a subsonic inlet relative Mach number 0.95 blade design case; representative of the tip of a transonic compressor rotor. The key geometric and aerodynamic design parameters, defining the inlet relative Mach number 0.95 blade datum design case are listed in Table 2.

M_{1rel}	α_{1rel}	M_{2rel}	α_{2rel}	t_{max}/c
0.95	60°	0.60	48°	4%
s/c	A_{x2}/A_{x1}	PC	$\psi=\Delta h_o/U^2$	A_t/A_1
0.80	0.95	40%	0.40	1.05

Table 2: Key geometric and aerodynamic parameters of a representative transonic rotor tip.

Fig. 5 plots the contours of the Mach number (at increments of 0.10) of the $M_{1rel} = 0.95$ transonic compressor blade at its design incidence. This is still a complex depiction of the flow field but can be broken down as follows by considering the contours highlighted in bold. First, the bold dot-dashed purple lines show the inlet area A_1 and throat area A_t that make up the important area ratio A_t/A_1 . The throat area A_t is defined here as the minimum cross-sectional area within the blade passage, when calculated normal to the mid-passage streamline, including the displacement from the boundary layer. As listed underneath the contour plot, at the design incidence A_t/A_1 is equal to 1.05. Second, the bold red solid lines indicate the sonic line. The shock terminates along the sonic line as the flow changes from supersonic to subsonic.

Hence, it provides a visual indicator of the shock's location. The shock can be seen to terminate before the throat. Third, with the bold dashed blue line, the Mach number contour of 0.75 is highlighted; showing the flow is well subsonic by the throat ($M_t = 0.73$). This results in the listed pressure rise across the shock of $P_t/P_1 = 1.18$, calculated by area averaging the pressure at the inlet and the throat plane. The lower the throat Mach number the higher the pressure rise across the shock and the stronger the resulting shock that forms.

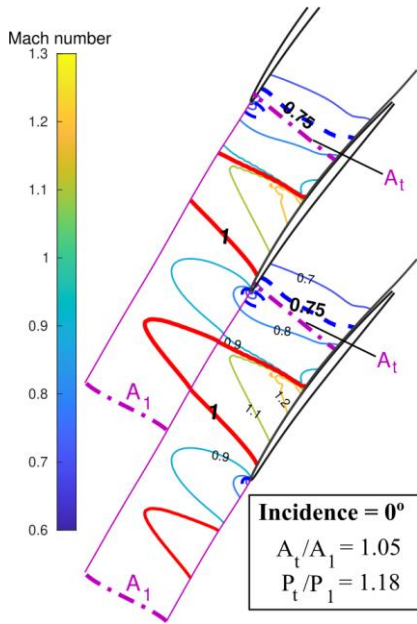


Fig. 5: $M_{1rel}=0.95$ transonic compressor blade Mach contours at the design incidence. The highlighted red solid line indicates the sonic line, the blue dashed line the Mach 0.75 contour and the dot-dashed purple line the streamtube area ratio A_t/A_1 .

Fig. 6 plots the transonic flow field of the same $M_{1rel} = 0.95$ transonic compressor blade now at (a) -1.2° negative incidence and (b) 2° positive incidence. To avoid unnecessarily overcomplicating the diagram, only the contours highlighted in bold are now shown when compared to Fig. 5. At negative incidence, as can be seen from Fig. 6(a), A_t/A_1 has decreased relative to the design incidence from 1.05 to 1.02. This is because the inlet area has increased. The Mach number at the throat is still subsonic but the Mach number contour of 0.75 shown by the bold dashed blue line, has moved further downstream. This means that the Mach number at the throat plane ($M_t = 0.84$) has gone up and this is further indicated by the fact that P_t/P_1 has decreased to 1.08. The shock accelerates slightly further into the passage and closer to the throat plane, yet still lies ahead of the throat plane. A small sonic bubble can be seen appearing below the pressure surface, which is where a normal shock forms coincident with the throat plane at the choking mass flow.

At positive incidence (Fig. 6(b)), A_t/A_1 can be seen to increase to 1.11 as the inlet area decreases. In addition, the $M=0.75$ contour now can be seen to lie ahead of the throat, meaning that the throat pressure has increased ($M_t = 0.69$ & $P_t/P_1 = 1.28$). This occurs because the shock moves closer to the leading edge resulting in a stronger pressure rise from the shock. As a result, it can be concluded that transonic flow feature A, i.e. the shock terminates

ahead of the throat plane, is satisfied when the throat pressure is subsonic. In other words, at all operating conditions except at the limiting choking condition.

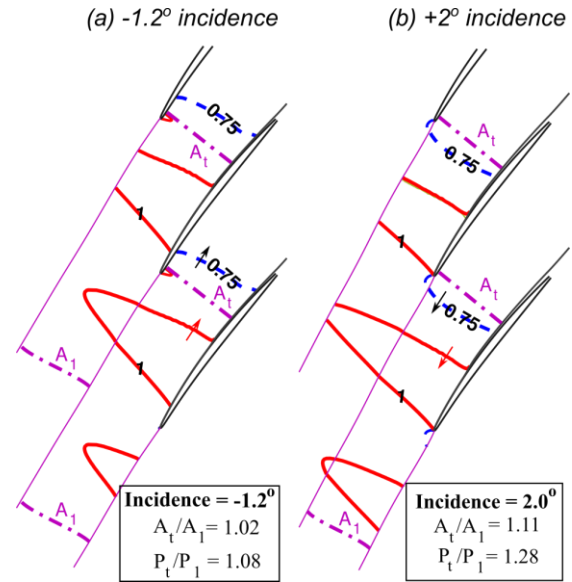


Fig. 6: $M_{1rel}=0.95$ transonic compressor blade Mach contours at (a) -1.2° negative incidence towards the choking condition & (b) 2° positive incidence towards maximum pressure rise.

In addition, for all incidences (Fig. 5 and Fig. 6) considered, the $M=0.75$ contours near the throat plane can be seen to be nearly parallel to the throat plane (i.e. normal to the midpassage flow); indicating that the pressure is relatively uniform by the throat plane, i.e. transonic flow feature B. This is because transonic blade rows achieve most of their pressure rise via a standing shock and do not require significant blade metal angle turning. In Section 5, it will be shown that this is the case even for highly loaded transonic compressors operating at loading coefficients ψ as high as 0.45.

Finally, to demonstrate the validity of transonic flow feature C, i.e. an effectively isentropic streamline exists within the blade passage, Fig. 7 is shown. Fig. 7(a) plots the contours of entropy loss coefficient $\zeta_s (=T_2\Delta s/(h_{01}-h_1))$ in the freestream from the shock structure at the design incidence. It can be seen that the loss gets created where the shock forms, and is largest nearer to the suction surface where the pre-shock Mach number is highest.

Fig. 7(b) plots the variation in the entropy loss coefficient ζ_s in the freestream from the shock, at the three incidences studied pitchwise along the outlet blade passage; shown as A_2 in Fig. 7(a). At the design incidence, shown by the dashed line, in the top 50% of the passage the loss is almost zero and the flow is effectively isentropic. This is because as the shock extends across the passage its pre-shock Mach number decreases to unity. The maximum loss is found at around 15% of the outlet passage width, where the pre-shock Mach number is 1.24, but that is a stagnation pressure loss of only 3% of P_1 , which is small when compared to the overall pressure rise achieved by the blade row of $P_2/P_1=1.2$. This makes sense since the rise in entropy from a normal shock scales by $(M^2-1)^3$ [25].

At negative incidence, shown by the solid line, the biggest difference can be seen near the pressure surface, where the small

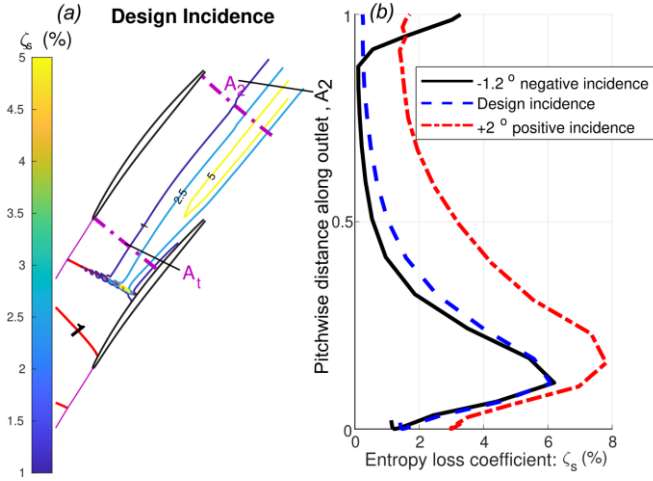


Fig. 7: $M_{1rel}=0.95$ transonic compressor blade (a) entropy loss coefficient contours at the design incidence & (b) entropy loss coefficient profiles for all three incidences considered along the passage outlet A_2 .

sonic bubble has appeared. The midpassage loss has decreased, whilst the peak freestream loss increases slightly, as the shock moves further into the passage. Once again these freestream losses are negligibly small. At positive incidence, the overall freestream loss across the passage can be seen to increase as the shock's strength in the freestream is near 1.30. However, the stagnation pressure loss is still on average less than 2% of P_1 and the total pressure rise P_2/P_1 has now increased to 1.41. Any further increase in positive incidence will come with significant shock-boundary layer separation. It can be concluded that an effective isentropic streamline is present in the case considered over most of the blade's operating range.

The presence of the three transonic flow features A, B & C, results in A_t/A_1 setting the transonic blade row's overall shock structure. To demonstrate this, Fig. 8, shows the change in pressure along three streamtubes within the blade passage at the design incidence. In the top figure, the flow field within the blade passage is shown with three streamtubes going through the passage and rotated to be horizontal for clarity. In the bottom figure, the static pressure along these streamtubes is plotted. The pressure along these streamtubes can be seen to increase just ahead of the leading edge, as the flow stagnates on the blade's leading edge nose. It then decreases, as it goes around the leading edge, accelerating supersonically until it is terminated by a shock ahead of the throat (transonic flow feature A); at which point the pressure increases abruptly. The flow then decelerates subsonically up to the outlet plane.

It can be seen by the size of the discontinuity in pressure that the green dashed streamtube traversing near the blade pressure surface, operates with a pre-shock Mach number of around 1.10, which comes about with negligible shock losses. Hence, it is an effectively isentropic streamtube connecting the inlet to the throat plane (transonic flow feature C), where it undergoes both an effectively isentropic expansion and compression. At the throat plane, shown by the bold purple line, the static pressure is the same across all three streamtubes showing that the pressure is virtually uniform (transonic flow feature B). As a result, because the pressure upstream of the blade and at the blade throat are

uniform and connected by an isentropic streamtube, for which 1D isentropic compressible area relations can be used, the pressure ratio between the throat and inlet plane boundaries becomes fixed by the area ratio A_t/A_1 . Hence, A_t/A_1 fixes the pressure boundary conditions across the shock and hence its overall strength.

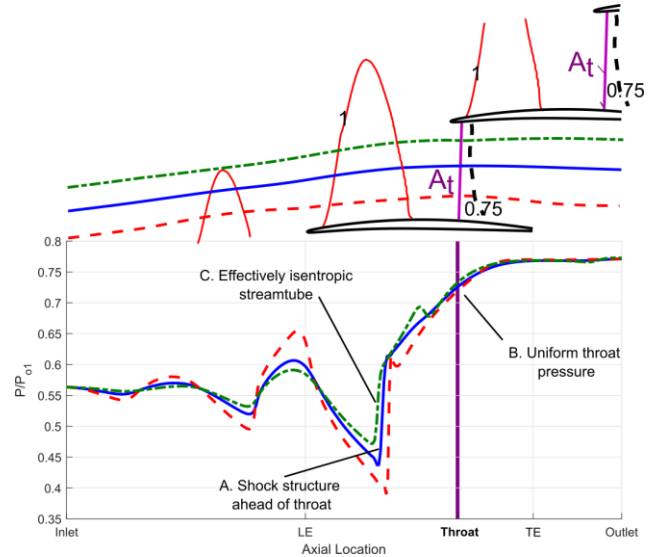


Fig. 8: $M_{1rel}=0.95$ transonic compressor blade pressure variations along three passage streamtubes showing how A_t/A_1 sets its overall shock structure. Contours of Mach number as well as the location of A_t are shown in top figure.

The validity of these three transonic flow features is demonstrated using Fig. 9, which has been derived using the web-based database published with this paper. Fig. 9 plots the pressure rise across the shock against A_t/A_1 for a range of representative transonic compressor designs, described in Section 2, each shown by a circular symbol, operating at six inlet relative Mach numbers. The throat area ratio has been calculated including the displacement from the boundary layer thickness. The inlet relative Mach number at which each design is operating is denoted by colour. These are: 1) $M_{1rel} = 0.85$ coloured in blue, 2) $M_{1rel} = 0.90$ coloured in orange, 3) $M_{1rel} = 0.95$ coloured in red, 4) $M_{1rel} = 1.0$ coloured in turquoise, 5) $M_{1rel} = 1.05$ coloured in green & 6) $M_{1rel} = 1.10$ coloured in yellow.

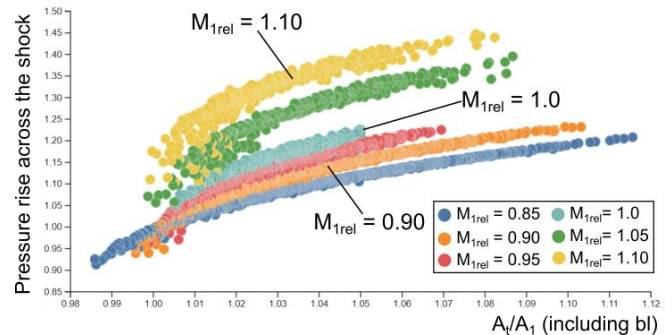


Fig. 9: Pressure rise across the shock for a wide range of transonic compressor designs covering $M_{1rel}=0.85-1.10$, each symbolised by a circular symbol and colour-coded by M_{1rel} .

In Fig. 9 it can be seen that all the designs corresponding to a particular M_{1rel} , despite them covering a wide range of aerodynamic and geometric parameters (summarised in Table 2),

lie on the curve determined by 1D compressible relations. At $M_{1rel} = 1.10$, there is slightly more scatter as the differences in the freestream loss between designs become more significant but are still second-order. This is not expected to remain the case for highly supersonic Mach numbers limiting the analysis presented in this paper to the transonic regime; defined here between $M_{1rel} = 0.85$ and 1.10. The fact that all the designs of a particular M_{1rel} follow the same curve proves that over the whole transonic regime and across a wide breadth of blade designs covering most of the civil transonic fans and compressors design space approaching a Mach number of unity, the transonic flow features A, B & C are applicable and hold true.

The reader is encouraged to explore the web-interactive online database provided with this paper by hovering over each design and examining how the Mach contour transonic flow field and pitchwise entropy loss coefficient, presented similarly to Fig. 6 & Fig. 7 in the online tool, adjusts whilst the transonic flow features A, B & C still hold.

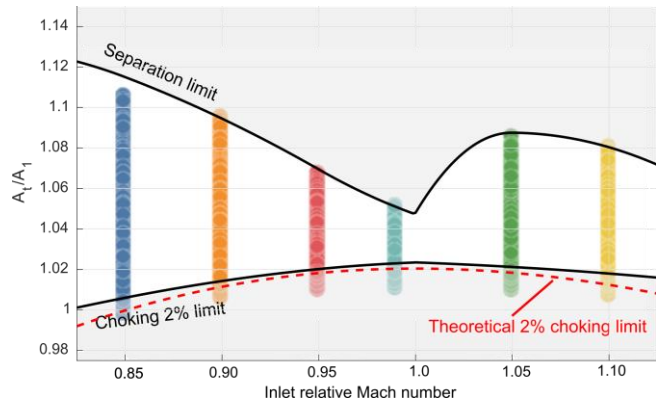


Fig. 10: Universal A_t/A_1 limits of shock-boundary layer separation and choking against inlet relative Mach number over the transonic Mach number regime. Each design symbolised by a circular symbol and colour-coded by M_{1rel} .

Finally Fig. 10 plots all designs (in circles) generated on a universal graph of A_t/A_1 against inlet relative Mach number. The black upper limit best-fit line indicates the values of shock-boundary layer separation above which MISES converged solutions were not possible due to significant separation being present. The lower black best-fit limit line signifies designs with less than 2% choking capacity. As a result, the upper and lower black limit lines indicate the limits in operable A_t/A_1 against the inlet relative Mach number for the full dataset considered. In red dashed the equivalent lower limit line is presented but derived theoretically from 1D compressible relations assuming a uniform Mach number of unity along the throat plane. The discrepancy observed between the two limit lines indicates that this assumption is not always accurate in the choking condition.

A pinch-point can be observed as the flow is approaching an inlet relative Mach number of unity, where only a 2.5% change in A_t/A_1 is the difference between shock-boundary layer separation and a choking capacity of 2%. The limit lines can be seen to widen again at supersonic Mach numbers. Fig. 10 is of critical importance for design purposes as the blade sections of any 3D transonic blade design can be assessed for their proximity to the choking or shock-boundary layer separation condition using this

graph. This will be done later in the paper to assess the level of fidelity necessary when calculating the 3D A_t/A_1 .

Summary

In summary, over the transonic regime, A_t/A_1 generally sets the pressure rise delivered by shock for the subsonic inlet Mach numbers approaching unity because of the three key flow features listed at the start of this section. If any of the flow features A, B & C are not present, then the assumption that A_t/A_1 primarily sets the pressure rise across the shock would not hold.

Examples of such cases would be: 1) at the maximum mass flow choking condition where the shock lies at the throat plane, which is opposite to conventional wisdom given that A_t/A_1 to date has been primarily used to determine this choking condition, 2) at design applications where very high loading coefficients ($\psi > 0.45$) are necessary and the pressure is no longer uniform by the throat plane and 3) at very high incidences, where the assumption of an effectively isentropic streamtube within the blade passage is no longer valid. However, most civil transonic compressor and fan cases over most of their operation do not fall into any of these categories and the three flow features A, B & C listed are present and adequately describe the transonic flow field.

Based on this analysis, Fig. 10 presents the most comprehensive set of limit lines of shock-boundary layer separation and choking published up to this point. Not only because it provides the only way of quantitatively assessing the point of shock-boundary layer separation in the literature, but also because predicting the choking capacity by the simple methods currently being taught and used in practice could be inaccurate.

4. EFFECT OF A_t/A_1 ON THE TRANSONIC FLOW FIELD

In the previous section, it was shown that A_t/A_1 fixes a blade's aero performance. This section aims to show that the effect of perturbing the geometry or the 3D radial contraction can be explained by tracking changes in A_t/A_1 . For conciseness, this section will only focus on the effects of perturbing the two crucial variables t_{max} and A_{xt}/A_{x1} .

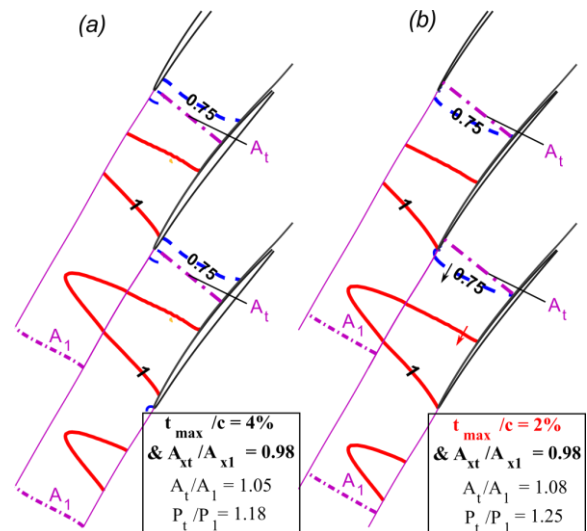


Fig. 11: Mach number contours of the $M_{1rel}=0.95$ transonic compressor (a) datum blade of $t_{max}/c=4\%$ & (b) that of the datum but with half-thickness.

It is well understood for an isolated transonic aerofoil that the effect of just reducing t_{max}/c is to decrease the amount of blade curvature up to the shock, resulting in a weaker shock. However, the opposite effect is observed when reducing t_{max}/c for transonic compressor blades, where the blade aerofoil is no longer isolated and a neighbouring blade exists. This is demonstrated using Fig. 11 that shows the important Mach number contours described previously of (a) the datum $M_{1rel}=0.95$ blade of $t_{max}/c = 4\%$, and (b) a blade of half the thickness $t_{max}/c=2\%$. It can be seen that the thinner blade has the $M=0.75$ contour ahead of the throat rather than behind it, as is the case for the datum. Hence, the thinner blade has a stronger shock which delivers a higher pressure rise, as evidenced by P_t/P_1 increasing from 1.18 to 1.25. This is the opposite aerodynamic behaviour to that expected from isolated aerofoils but can be explained simply by examining the associated changes in A_t/A_1 .

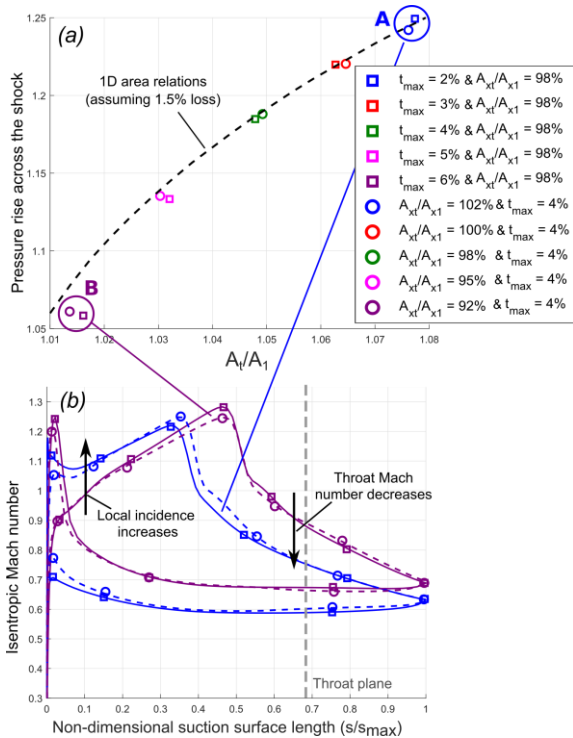


Fig. 12: $M_{1rel}=0.95$ transonic compressor blade (a) pressure rise across the shock against A_t/A_1 & (b) isentropic Mach numbers of compressor blades of varying t_{max} and A_{xt}/A_{x1} .

Fig. 12 is based on the database generated and supports this argument. In Fig. 12(a), P_t/P_1 against A_t/A_1 is plotted, with the design cases of varying t_{max}/c from 2% to 6%, whilst keeping $A_{xt}/A_{x1} = 0.98$ constant, shown by the square symbols. It can be seen that as t_{max}/c is reduced from 6% to 2%, A_t/A_1 increases from 1.015 to 1.08. This is because the result of reducing t_{max} is to increase the geometric throat area o . By extension, this results in an increase in A_t/A_1 . As a result, because A_t/A_1 sets the pressure rise boundary conditions across the shock, the thinner blade with a higher A_t/A_1 has to deliver a larger pressure ratio via a stronger shock.

To understand how the flow field adjusts to achieve this higher pressure rise across the shock, Fig. 12(b) plots the resulting isentropic Mach number for A: $t_{max}/c = 2\%$ (blue solid line with

square symbols) and B: $t_{max}/c = 6\%$ (purple solid line with square symbols). It can be seen that the thinner blade in blue, has a lower throat Mach number and achieves this despite having less curvature up to the shock foot, by operating at a higher local incidence. This is physically achieved by subtle changes in the stagnation streamlines as it impinges onto the blade's leading edge.

The same study is performed but now keeping the blade geometry fixed and just perturbing the radial contraction up to the throat A_{xt}/A_{x1} . During this study, A_{xt}/A_{x1} is changed from 102% to 92%, while the overall radial contraction A_{x2}/A_{x1} is kept at 95% and $t_{max}/c = 4\%$. These cases are shown by the circular symbols in Fig. 12(a), and with the dashed lines with circles in Fig. 12(b).

In Fig. 12(a) the circular and square symbols fall virtually on top of each other and lie on the black dashed curve, which has been derived theoretically by using 1D area ratio compressible relations and assuming an average freestream loss of 1.5%. This level of freestream loss is similar to what was observed previously in Fig. 7. Hence, as expected the pressure rise across the shock is universally set by A_t/A_1 ; irrespective of whether the throat area is changed via a geometric blade change, e.g. an increase in t_{max}/c , or a radial streamtube height change. Moreover, in Fig. 12(b), designs sharing the same A_t/A_1 exhibit comparable isentropic Mach number distributions, regardless of whether t_{max}/c (solid

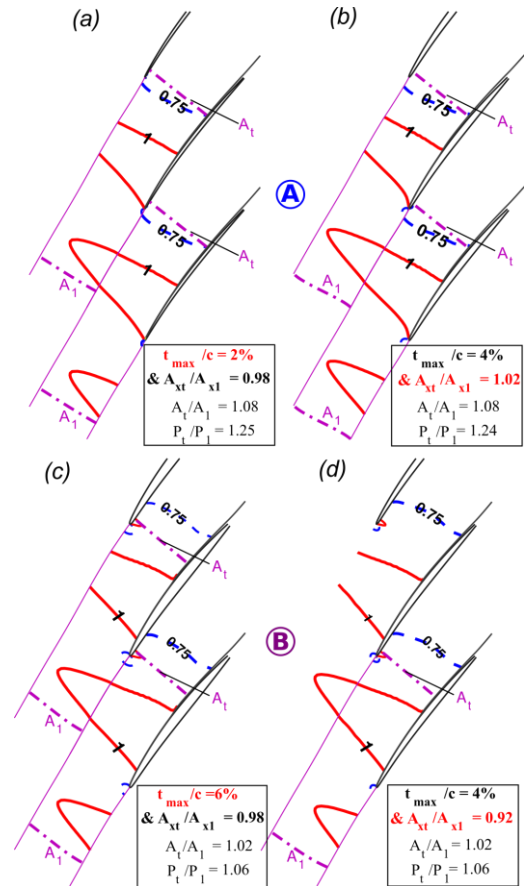


Fig. 13: Mach number contours of the $M_{1rel}=0.95$ transonic compressor (a) datum blade of half-thickness, (b) datum blade with a radial streamtube expansion of $A_{xt}/A_{x1} = 1.02$, (c) datum blade of 1.5 times the thickness & (d) datum blade with a radial streamtube contraction of $A_{xt}/A_{x1} = 0.92$.

lines with squares) or A_{xt}/A_{x1} (dashed lines with circles) is perturbed in the given design.

Finally, in Fig. 13, it is shown that the transonic flow fields of blades of the same A_t/A_1 , achieved through either a change in maximum thickness (t_{max}/c) or radial contraction at the throat plane (A_{xt}/A_{x1}), are similar despite the blade geometries being different. The transonic compressor blade of $t_{max}/c = 2\%$ & $A_{xt}/A_{x1}=98\%$, Fig. 13(a), has virtually the same $A_t/A_1 = 1.08$, and therefore the same Mach contour pattern as the one operating with $A_{xt}/A_{x1}=102\%$ & $t_{max}/c = 4\%$, Fig. 13(b), despite having different thicknesses (2% vs 4%) and radial contractions (0.98 vs 1.02). The same is true for the transonic blade of $t_{max}/c = 6\%$ & $A_{xt}/A_{x1}=98\%$, Fig. 13(c), and the one operating with $A_{xt}/A_{x1}=92\%$ & $t_{max}/c = 4\%$, Fig. 13(d), that have the same A_t/A_1 . Both form a similar small pressure surface sonic bubble around the leading edge as they are approaching the choking condition, as expected from the absolute value of $A_t/A_1 = 1.02$ being much smaller than for the blades (a) and (b) shown on the top of Fig. 13.

Summary

In summary, for transonic Mach numbers, the effect of perturbing the datum blades on the transonic flow field can be explained simply by tracking the change in A_t/A_1 ; a 1D type of assessment. Hence, in the example shown here the effect of thickening the blade or contracting the radial streamtubes on the shock is similar despite the difference in blade geometry; provided they block the throat area by the same amount.

The same conclusions can be derived from perturbing the other key geometric variables, for example: s/c (pitch-to-chord), χ_1 (inlet blade metal angle) & χ_2 (outlet blade metal angle), which can be found and studied online in the following interactive database demo².

5. DEPENDENCE OF SECTIONAL DESIGN ON A_t/A_1

In blade sectional design, the important aerodynamic property to control for a given desired pressure rise, is the pre-shock Mach number. This section explores whether for a given A_t/A_1 , which as discussed in Section 3 sets the pressure rise across the shock, there are specific geometric and aerodynamic design parameters that minimise the required pre-shock Mach number and are hence aerodynamically desirable.

To make this assessment the full database of transonic compressor designs operating at $M_{1rel} = 0.95$, published online in parallel with this paper³, is analysed. Fig. 14 plots the pre-shock Mach number against A_t/A_1 of representative transonic compressor designs operating at $M_{1rel} = 0.95$. The pre-shock Mach number plotted on the y-axis is calculated as the area average across the shock. Once again, the area ratio A_t/A_1 on the x-axis has been calculated including the displacement from the boundary layer thickness.

Fig. 14(a) displays all transonic compressor designs generated operating at $M_{1rel} = 0.95$ (more than 1700) covering the full sweep of key aerodynamic and geometric parameters summarised in Table 1. These cover most of a civil compressor

and fan's potential design space. It can be seen that there is a clear linear relationship between the pre-shock Mach number and A_t/A_1 . This is because to first order it is the pressure rise across the shock controlled by A_t/A_1 that sets the pre-shock Mach number. However, there is some scatter present that will now be explained.

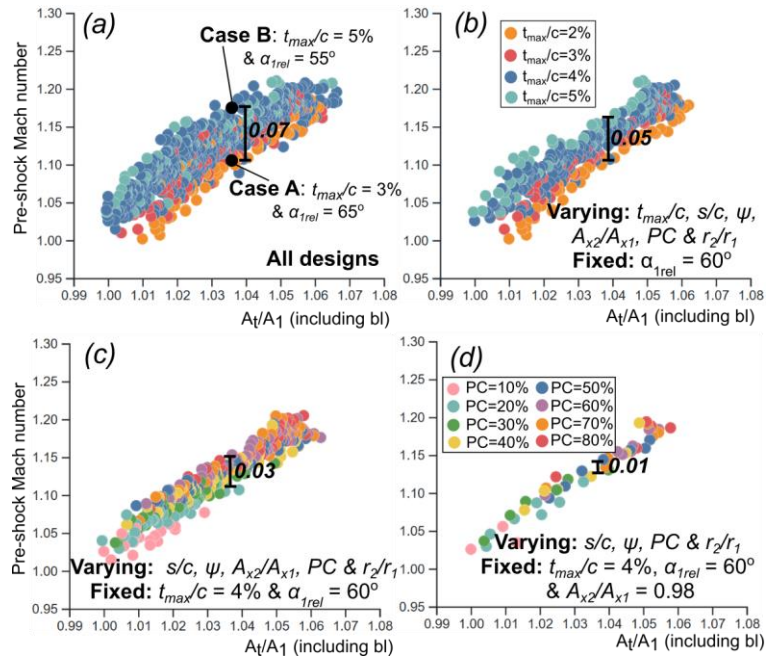


Fig. 14: Pre-shock Mach number against A_t/A_1 for (a) all $M_{1rel} = 0.95$ designs of varying α_{1rel} , t_{max}/c , s/c , ψ , A_{x2}/A_{x1} , PC & r_2/r_1 listed in Table 1, (b) designs of fixed $\alpha_{1rel} = 60^\circ$, (c) designs of fixed $\alpha_{1rel} = 60^\circ$ and $t_{max}/c = 4\%$ & (d) designs of fixed $\alpha_{1rel} = 60^\circ$, $t_{max}/c = 4\%$ & $A_{x2}/A_{x1} = 0.98$. Designs in (a) & (b) are colour-coded based on t_{max}/c , and designs in (c) & (d) are colour-coded based on PC .

To explore the root cause of the observed scatter in the pre-shock Mach number the interactive web-based demo accompanying this paper is used which allows the user to select fixed values for some of the geometric and aerodynamic design parameters listed in Table 1, exposing the impact on the scatter of the other unfixed parameters. More information on how to do this using the web-interactive online database will be explained in the final section of this paper.

For example, by fixing the inlet relative flow angle $\alpha_{1rel} = 60^\circ$, the impact of thickness-to-chord t_{max}/c , pitch-to-chord, s/c , loading coefficient, ψ and overall radial contraction A_{x2}/A_{x1} , for different PC blade designs (shown in Fig. 4) can be studied. This example case is shown in Fig. 14(b), where it can be seen that this design subset has reduced the scatter by about 30%. If t_{max}/c is also fixed to be 4%, as shown in Fig. 14(c), the scatter is further reduced by another 40%. Finally, if A_{x2}/A_{x1} is also fixed, as depicted in Fig. 14(d), all remaining designs, which include designs of varying s/c , ψ & PC fall on a single line with nearly no scatter present.

To understand the reason for the difference in pre-shock Mach number arising from differences in α_{1rel} and t_{max}/c , the two design Cases A and B indicated in Fig. 14(a) will be compared. These two designs are of the same $A_t/A_1 = 1.035$, yet show a significant difference in pre-shock Mach number. Case A has a

² https://whittle.digital/2024/Nature_of_Transonic_Compressor_Flow/M95_Case_I/

³ https://whittle.digital/2024/Nature_of_Transonic_Compressor_Flow/M95/

$t_{max}/c = 3\%$, $PC = 30\%$ and operates with $\alpha_{1rel} = 65^\circ$, and Case B has a $t_{max}/c = 5\%$, $PC = 60\%$ and operates with $\alpha_{1rel} = 55^\circ$. All other key geometric and aerodynamic properties have been kept the same between the two designs: $s/c = 0.80$, $\psi = 0.40$, $r_2/r_1 = 1.0$ and $A_{x2}/A_{x1} = 0.95$.

The blade profiles and Mach contours of Cases A and B are shown in Fig. 15. It can be seen that because A_t/A_1 is the same, the $M=0.75$ contour is located at the same position relative to the throat within the blade passage. Hence, the pressure rise delivered by the shock $P_2/P_1 = 1.15$ is the same; despite Case A being a much thinner blade and of significantly higher stagger than Case B.

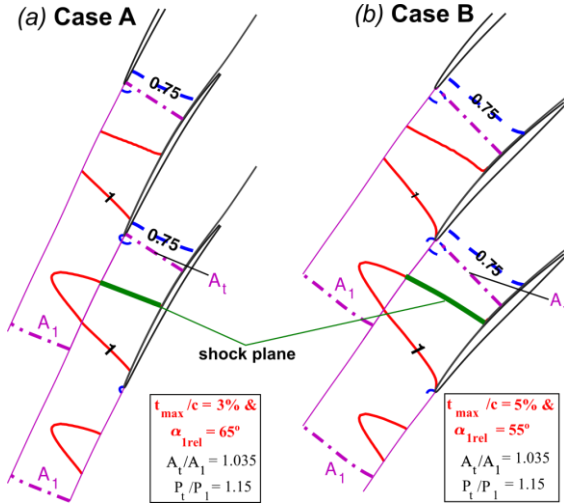


Fig. 15: (a) Case A & (b) Case B (indicated in Fig. 14(a)) blade profiles and Mach number contours.

Fig. 16 shows the change in (a) pre-shock Mach number and (b) the associated loss generated along the shock plane indicated in Fig. 15. It can be seen that the shock of design Case B (red dashed), has a larger variation in pre-shock Mach number across it, and a larger peak Mach number close to the blade surface when compared to design Case A (blue solid), where the pre-shock Mach number is more uniform and on average lower (Fig. 16(a)). This results in a higher loss being generated locally closer to the blade surface (Fig. 16(b)).

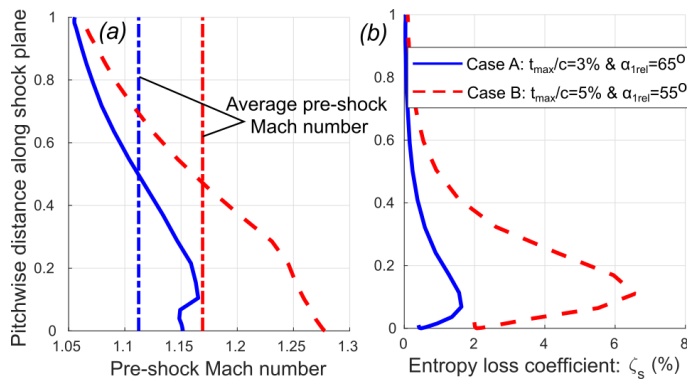


Fig. 16: (a) Isentropic Mach number & (b) freestream pressure loss along the passage outlet for Case A (blue solid) and Case B (red dashed) (indicated in Fig. 14(a)).

It should be noted that in both cases, away from the blade surface an effectively isentropic streamline still exists (Fig. 16(b)) and hence A_t/A_1 still sets the pressure rise P_2/P_1 across it. However,

in Case B the additional pressure rise delivered by the stronger shock is negated by the increase in pressure loss stemming from the higher loss being generated.

The difference in pre-shock Mach number just observed between design Cases A & B is because of the two compounding effects of thickness and inlet relative flow angle on the throat area.

First, introducing blade thickness means more of the geometric throat area o is blocked for a given camber distribution. As a result, camber needs to be added up to the throat to negate this effect and keep A_t/A_1 constant. This is because, going back to Fig. 2, $A_t/A_1 = o/A_1 \times A_{xt}/A_{x1}$. Similarly, an increase in the radial contraction A_{xt}/A_{x1} , although not shown in this example, would have the same effect.

Second, a reduction in the inlet relative flow angle increases the inlet area A_1 , because A_1 is equal to the pitch s times the cosine of α_{1rel} . This means that to maintain the same A_t/A_1 , o has to increase again, which once again requires the introduction of more camber up to the throat.

For these reasons, the overall change in blade metal angle up to the shock for transonic design Case B is $\chi_{sh} - \chi_1 = 9^\circ$, which is 3.5° greater than the equivalent of Case A, where $\chi_{sh} - \chi_1 = 5.5^\circ$. This increased blade metal angle at the point where the shock terminates is the reason for the local increase in pre-shock Mach number and associated loss close to the surface that is responsible for the scatter observed in Fig. 14.

A higher pre-shock Mach number for a given A_t/A_1 will result in an earlier onset of shock-boundary layer separation. This is because independent of inlet relative Mach number extensive transonic compressor cascade tests, summarised by Starcken [2], show that there is a limit in pre-shock Mach number on the surface of around 1.35 where the measured loss increases rapidly due to shock-boundary layer separation. This is also evident by highlighting designs at the boundary of shock-boundary layer separation in the interactive transonic dataset published online and visualising the pre-shock Mach number along the shock plane for each design similar to Fig. 16.

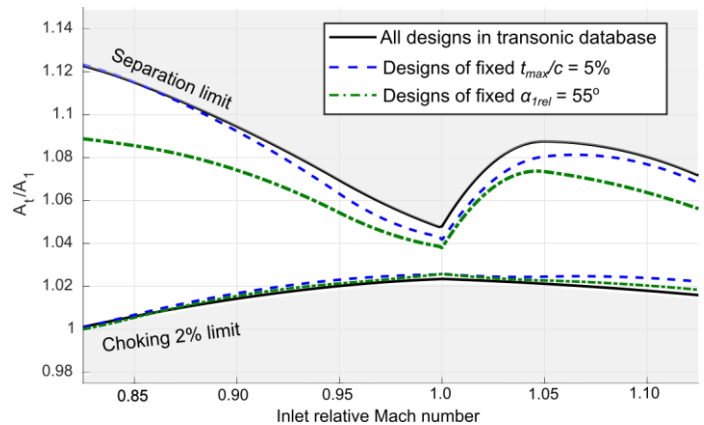


Fig. 17: A_t/A_1 limits of shock-boundary layer separation and choking against inlet relative Mach number over the transonic Mach number regime for all designs in the transonic database (black), designs of a fixed $t_{max}/c = 5\%$ (blue dashed) & designs of a fixed $\alpha_{1rel} = 55^\circ$ (green dot-dashed).

To demonstrate the earlier onset of shock-boundary layer separation for low stagger and thick blades just discussed, Fig. 17 has been produced (similarly to Fig. 10) using only a selected

subset of the designs within the dataset published. In black the shock-boundary layer separation and choking limit lines for all the designs, as before in Fig. 10, are shown. In blue dashed and green dot-dashed, the subset of designs with $t_{max}/c=5\%$ and $\alpha_{1rel}=55^\circ$ fixed are shown respectively. It can be seen that the range of A_t/A_1 possible designs within the limit lines reduces. This is expected from the preceding discussion that low stagger and thick blades have a higher average pre-shock Mach number for a given A_t/A_1 when compared to thin and high stagger blades.

Whilst only two subsets of designs are shown here, the reader can explore different subsets of designs using the published web-interactive transonic dataset. Generally, the A_t/A_1 limit lines are most sensitive to t_{max}/c , α_{1rel} and A_{x2}/A_{x1} ; parameters which are usually set during the preliminary design phase. No significant sensitivity was observed to the other design parameters investigated.

Summary

In summary, the pre-shock Mach number is to first order dependent on the 1D value of A_t/A_1 . To second order, the pre-shock Mach number is dependent on the geometric design parameters t_{max}/c , α_{1rel} and A_{x2}/A_{x1} , as they were shown to induce the largest scatter in Fig. 14. The reason is that these are the design parameters that when perturbed affect A_t/A_1 for a given camber distribution the most. Nevertheless, even then significant differences are only observed at the extreme ends of the design space. In general, low stagger and thick blades are shown to be aerodynamically undesirable, which matches with design experience as transonic rotors in the front of the compressor are usually of high reaction (i.e. high stagger) and made as thin as possible.

On the other hand, as can be concluded from Fig. 14(d), a blade section's pre-shock Mach number is weakly dependent on the geometric differences that come about from varying s/c & ψ and is purely a function of A_t/A_1 . Despite the geometries of varying s/c & ψ being of a different PC at a given A_t/A_1 , as indicated by the colour coding in Fig. 14(d), it can be deduced that the resulting differences in the local suction surface camber and loss between designs are small and have little to no consequence on the pre-shock Mach number.

It is worth noting that the key variables t_{max}/c , α_{1rel} and A_{x2}/A_{x1} would all be set in the preliminary design phase before the detailed 3D design. Hence, these findings suggest that at the point of the 3D design, detailed blade sectional profiling is not important, and the purpose of the sectional detailed design phase should be solely to make the desired changes in the real spanwise 3D A_t/A_1 . In fact, this analysis shows that during 3D design a section's performance can be purely assessed by accurately extracting a single value for A_t/A_1 .

Even though not presented for conciseness, the same conclusions can be drawn for all the other subsonic Mach numbers approaching unity. These can be investigated individually by using the web-based visualisation database accompanying this paper, where variations in loss and pre-shock Mach number along the shock plane for different designs can be examined similarly to Fig. 16.

6. 3D NATURE OF TRANSONIC COMPRESSOR FLOW

In the previous sections, the radial contraction across the blade passage was a free independent variable. In practice, however, this is not the case, as changes in the 3D blade geometry will also result in changes in the 3D radial flow within the blade passage. This section explores the importance of accounting for this effect.

Fig. 18(a) presents the spanwise distribution of A_t/A_1 from hub-to-tip of five different transonic rotor designs derived using 3D CFD plotted on the A_t/A_1 versus inlet relative Mach number universal limit graph presented previously in Fig. 10. The blue spanwise A_t/A_1 line with crosses is indicative of an optimal 'aerodynamically balanced' transonic rotor design; one which operates at every spanwise section with an A_t/A_1 value which lies between its choking and shock-boundary layer separation limit over the widest range of operating conditions. The details of this representative transonic rotor, and the 3D CFD setup can be read in [13], where it was shown that an aerodynamically balanced design results in a near percentage point improvement in efficiency and more than a 15% increase in operating range over multiple blade speeds, when compared to an unbalanced design.

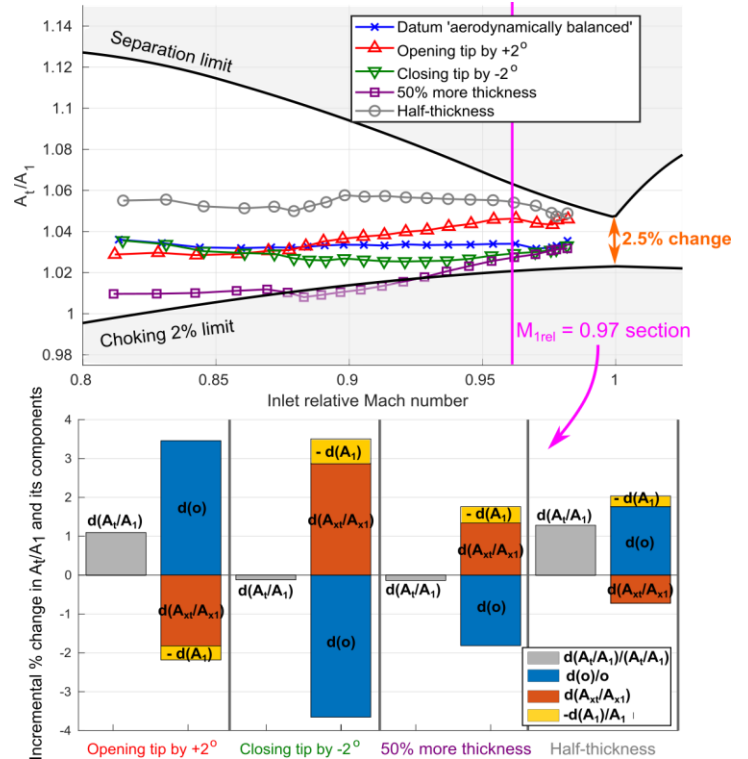


Fig. 18: (a) Spanwise distribution of A_t/A_1 for a datum representative aerodynamically balanced transonic rotor design and four other rotors where spanwise perturbations in stagger and thickness have been applied & **(b)** incremental change in A_t/A_1 and its constituent components for the $M_{1rel} = 0.97$ blade section of each spanwise perturbed rotor relative to the datum.

The remaining four rotor designs presented in Fig. 18(a) are cases where a perturbation has been applied up the span to the datum aerodynamically balanced rotor and the designs rerun in 3D CFD to the same mass flow condition. In red with upward-pointing triangles is the case where the blade is opened by 2° at the tip; with it linearly decreasing back to zero at the hub. In green

with downward-pointing triangles is the opposite case where the blade is closed by 2° at the tip. Finally, in purple with squares and grey with circles are the cases where the blade has been thickened by 50% and thinned by 50% respectively.

Revisiting Fig. 1, it can be seen that a change in the 3D rotors spanwise sectional design, does not only change the geometric throat area, o , but also the behaviour of the 3D radial streamtube enclosing that section. The latter varies by 1) the radial streamtube contracting or expanding by the throat plane, i.e. A_{xt}/A_{x1} and 2) by shifting its inlet radius and altering the inlet area A_I . In this case, the pressure rise from the change in radius is negligible and hence neglected in this analysis for simplicity. As indicated in Fig. 2, these three constituent components when multiplied together set the overall A_t/A_I .

Fig. 18(b) plots a bar chart of the percentage change in A_t/A_I and its constituent components for the $M_{I,rel} = 0.97$ blade section of each spanwise perturbed rotor relative to the datum aerodynamically balanced design. For small incremental changes: $d(A_t/A_I)/(A_t/A_I) = d(o)/o + d(A_{xt}/A_{x1})/(A_{xt}/A_{x1}) - dA_I/A_I$; i.e. the grey bar is equal to the sum of the blue, orange and yellow bar.

Overall, it can be seen that despite the significant changes in o applied, the change in A_t/A_I is not as significant for all perturbation cases considered. In fact, the change in A_t/A_I is nearly negligible for the cases where the blade tip is closed by 2° and increased by 50% in thickness. This is primarily because of the change in A_{xt}/A_{x1} , which always acts to negate any change in the geometry, o . The 3D flow mechanism of ‘transonic relief’ behind this phenomenon has been explained in [12]. It is this mechanism that allows transonic rotors to operate with a significant incidence range and makes rotors tolerant to manufacturing variations and small design errors.

Summary

In summary, considering changes in the sectional geometry in isolation from the changes in 3D radial flow within the passage is inherently incorrect, because whenever a sectional geometry change is applied there is also an associated equal order of magnitude change in A_{xt}/A_{x1} . This 3D nature of A_t/A_I is the reason why large geometric changes are required to make relatively small changes in A_t/A_I . Hence, to be able to make appreciable design changes such as changing a section’s A_t/A_I , it is important to take into account this 3D effect during the design process as described in more detail in [13].

7. ACCURATELY EXTRACTING 3D A_t/A_I FOR DESIGN

Up to this point, this paper has shown that the performance of a given section of a rotor can be assessed, after the preliminary design features have been set, purely using A_t/A_I . However, the key to determining the value of A_t/A_I is extracting it accurately enough in an appropriate 3D environment. This section discusses the implications of this for the design of the front transonic stages of multistage compressors.

In multistage compressor design, at the early design phase lower-order 3D streamline curvature throughflow methods are used to explore and eventually set the blade rotational speed, hub and casing lines, target inlet and outlet flow angles across the blade row, as well as provide initial estimates for the maximum

thickness-to-chord and blade number. This is done to achieve two design objectives: 1) the desired matching between the front transonic and rear subsonic stages but also 2) to provide appropriate boundary conditions for the design of an efficient rotor or stator blade. Both are key to the successful development of any compressor.

To assess the feasibility of the latter, when it comes to the front transonic stages operating with shocks, it is important to get an accurate assessment of spanwise A_t/A_I . The reason for this is twofold and can be derived from the discussion already made in Section 6. First, because when approaching the sonic condition only a 2.5% variation in A_t/A_I can be the difference between choking and shock boundary layer separation. Second, because to achieve even modest changes in A_t/A_I large changes in the blade geometry are required, which means that starting with an unbalanced transonic rotor design could be hard to fix in the 3D detailed design phase.

Particularly for the design of new radically different multistage compressors, where previous experience is not there to guide the initial transonic design of the front stages, getting an accurate calculation of A_t/A_I quickly, and subsequently assessing whether it is aerodynamically balanced using the improved shock-boundary layer separation and choking limits presented in this paper could play a key part for the rapid exploration and the successful development of future more efficient multistage compressors.

However, getting an imprecise calculation for A_t/A_I could actually be misleading. Hence, the question is what the appropriate 3D computational environment is to make such an assessment. Are low-order methods such as the throughflow adequate or should higher fidelity 3D CFD be brought in earlier in the design process?

To test this, the A_t/A_I spanwise distribution of the representative transonic civil multistage front stage rotor redesigned using 3D CFD in [13] to be ‘aerodynamically balanced’, as already shown in Fig. 18, is compared directly to that predicted by the streamline curvature throughflow SLEQ [24].

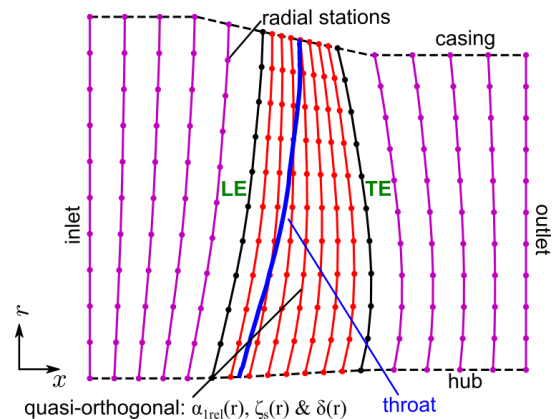


Fig. 19: Schematic of streamline curvature throughflow (SLEQ) grid and throat location for the representative transonic civil rotor redesigned to be aerodynamically balanced in [13].

Fig. 19 shows the setup for the equivalent SLEQ grid domain, which is made to exactly match the outer domain of the 3D CFD, i.e. an isolated rotor is run with the same inlet and outlet

boundaries and hub and casing lines as the 3D CFD. It can be seen that the SLEQ grid is defined by a number of quasi-orthogonals and radial stations, which can be chosen by the user. In the specific example shown in Fig. 19, the grid has been set up to have 5 inlet and outlet duct quasi-orthogonals (purple lines), 7 internal curved quasi-orthogonals within the blade passage (red lines) and 11 radial stations (dots).

Along each quasi-orthogonal and radial station, three properties are defined spanwise and these are: 1) the inlet relative flow angle: α_{1rel} , 2) the entropy loss coefficient: ζ_s and 3) the blockage from the blade's thickness: δ . To give the throughflow the best possible opportunity to calculate 3D A_t/A_1 accurately, in the first instance, these have been extracted directly from the 3D CFD.

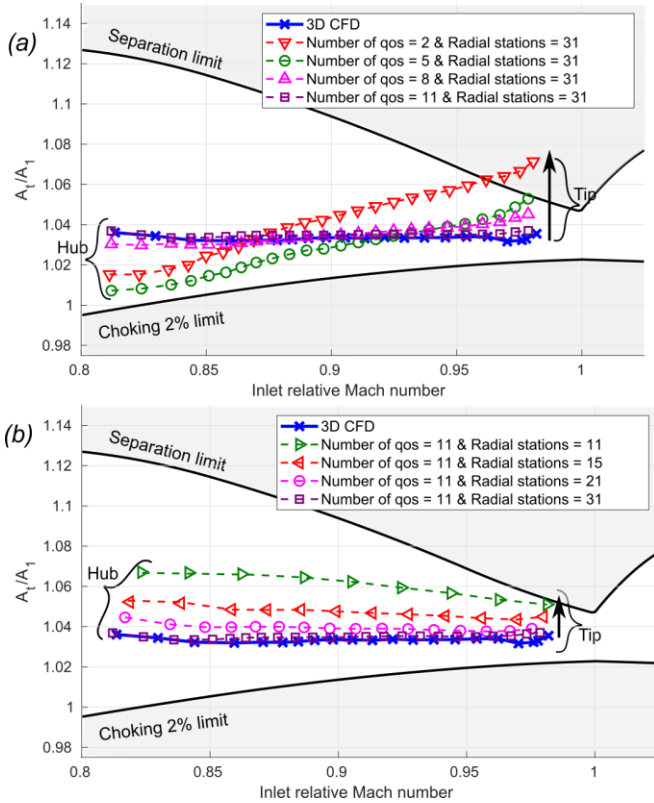


Fig. 20: Spanwise A_t/A_1 distribution from hub-to-tip of the aerodynamically balanced transonic front stage compressor rotor, as predicted by the throughflow streamline curvature method using a different number of (a) internal quasi-orthogonals and (b) radial stations. The 3D CFD A_t/A_1 distribution is plotted for comparison.

Fig. 20, plots the spanwise A_t/A_1 distribution as calculated in SLEQ using a variety of (a) quasi-orthogonals and (b) radial station setups, and compares it against that predicted by the 3D CFD. In SLEQ, A_t/A_1 has been calculated as the ratio of $(\rho_1 V_{1rel})/(\rho_t V_{trel})$ along the throat line shown in blue in Fig. 19, at each radial spanwise point; similar to how it was done in the 3D CFD [13].

It can be deduced that if too few quasi-orthogonals or radial stations are used the difference between the A_t/A_1 distributions calculated in SLEQ compared to that from the 3D CFD can become significant. For example, it can be seen from Fig. 20(a) that if 8 or fewer quasi-orthogonals are used to simulate the

internal blade passage, the throughflow would incorrectly predict an unbalanced profile. This unbalanced spanwise profile would have too high an A_t/A_1 at the tip; close to or even exceeding the shock-boundary layer separation limit. This would mislead the designer to either change the tip inlet relative flow angles into the rotor domain to increase A_1 or change the geometry to reduce α , even though the design would have been already optimum and aerodynamically balanced.

The same can be observed in Fig. 20(b), where having fewer than 21 radial stations, would again predict too high of an A_t/A_1 . This, for example, could suggest that the blade can be thickened further, when in fact this would choke the blade.

For SLEQ to match the 3D CFD, a minimum of 11 internal blade passage quasi-orthogonals and 31 radial stations are required. Discretising the domain any further does not affect the prediction of A_t/A_1 . This indicates the importance of discretising the domain to a high enough accuracy when using throughflows. It should be noted that this level of discretisation is much higher than the one shown in Fig. 19 or typically used.

However, the largest potential error in using a throughflow does not come about from the discretisation but from the three inputs to the throughflow: 1) α_{1rel} , 2) ζ_s and 3) δ . For the SLEQ cases plotted in Fig. 20 these inputs have been taken directly from the 3D CFD and hence provided there is high enough discretisation an agreement is expected. Nevertheless, in practice, there is an uncertainty related to each of these inputs.

The uncertainty in the α_{1rel} set inside the blade passage is related to errors arising from predicting the deviation of a given blade design. The uncertainty in ζ_s is related to errors in predicting the loss generated within the blade row. Finally, the uncertainty in δ comes from the additional blockage induced by the boundary layer. In fact, just to get SLEQ and 3D CFD to match in Fig. 20, the blockage from the blade thickness had to be increased by an additional 15% to account for the boundary layer. In the presence of strong shocks and thin blades, this additional blockage would be even greater.

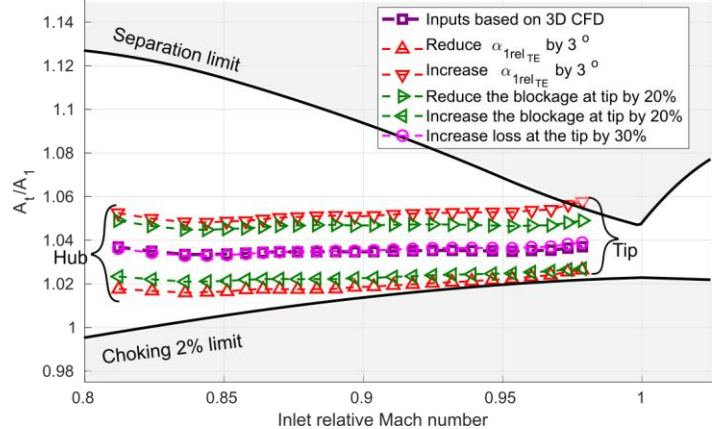


Fig. 21: Spanwise A_t/A_1 distribution from hub-to-tip of a transonic front stage compressor rotor, as predicted by the throughflow streamline curvature method using inputs for α_{1rel} , ζ_s & δ directly from the 3D CFD and after applying perturbations to those inputs.

To assess the impact of this uncertainty on the predictive capability of the throughflow, the appropriately discretised SLEQ setup (11 quasi-orthogonals & 31 radial stations) is used but now with perturbations applied to each of the input variables. In Fig.

21 in red, the effect of increasing/decreasing the inlet relative flow angle at the trailing edge by 3° is shown. This is applied as a linear change from the leading edge, where α_{1rel} is kept the same, to the trailing edge, and aims to simulate the effect of incorrectly predicting deviation. In green, the effect of reducing/increasing the blockage at the tip of the blade is shown from incorrectly predicting the boundary blockage at the tip by 20% where the blades are thin and shocks are present. This is applied as a linear change from hub to tip. Finally, the effect of increasing the tip loss by 30%, once again linearly from hub to tip, is shown in pink.

Overall, it can be seen that incorrectly predicting deviation or the blockage from the boundary layer can have a significant effect on the prediction of A_r/A_l . Similar to the discretisation examples shown in Fig. 20, the error is large enough that it can potentially mislead the transonic design and lead to unbalanced designs. On the other hand, the prediction of A_r/A_l is weakly dependent on loss generated at the tip. This insensitivity of A_r/A_l to loss is expected from the discussion already made in Section 5.

Summary

In summary, provided an appropriate level of discretisation is used and the inputs are calculated correctly to a high enough level of precision, lower-order streamline curvature throughflow methods can theoretically predict the A_r/A_l spanwise distribution of a transonic rotor. However, particularly the sensitivity of the calculation to deviation and boundary layer blockage, makes it an impractical lower-order design method, as it is not accurate enough and may even mislead the design process. This is important because it is at this early design stage, when appropriate boundary conditions and key geometric parameters for the design of an efficient transonic blade need to be set.

Getting this initial design step correct is critical for the successful development of any multistage compressor, especially in the exploration stage where radically new designs need to be assessed quickly. An alternative 3D early design method using higher fidelity 3D CFD is required and this will be presented next.

8. EARLY DESIGN METHOD BASED ON A_r/A_l DATASET

Lower-order early design methods such as throughflows, despite not being accurate enough in their calculation of A_r/A_l , have the benefit that blade sections do not need to be generated but are simulated by a group of physical inputs. This allows for any boundary condition to be assessed without a 3D blade needing to be generated, which is what would be required if 3D CFD were to be brought in for accuracy already at this stage. Hence, this section proposes generating the blade sections for a given set of boundary conditions and early design choices we wish to explore using the dataset of blades provided as a link within this paper.

For the generation of a given blade section the design space is parameterised based on three key groups of aerodynamic and geometric parameters. The first group, M_{1rel} and α_{1rel} , sets the inlet relative Mach number triangle. The second group including ψ and A_{x2}/A_{x1} set the outlet relative Mach number triangle. Finally, the third group sets early design choices such as t_{max}/c and s/c . The online database published with this paper has the 10,000 blade designs grouped using this set of key geometric and aerodynamic parameters. These parameters can be isolated by selecting the appropriate tabs on the web-interactive demo to restrict the designs possible.

The new early design method proposed aims to use this A_r/A_l database to generate the transonic sections of an initial rotor design for any given set of boundary conditions and early design choices. This initial design can then be run and checked in 3D CFD, which is now quick for single-blade rows. Fig. 22 shows the process for deriving the tip section, operating at an inlet relative Mach number close to unity, for the aerodynamically balanced front-stage civil rotor blade considered in this paper. Its key geometric and aerodynamic properties are shown in Table 3. The design objective is to find a sonic section within the database that matches these boundary conditions and importantly has an $A_r/A_l = 1.03$; i.e. between the two limits of shock-boundary layer separation and choking.

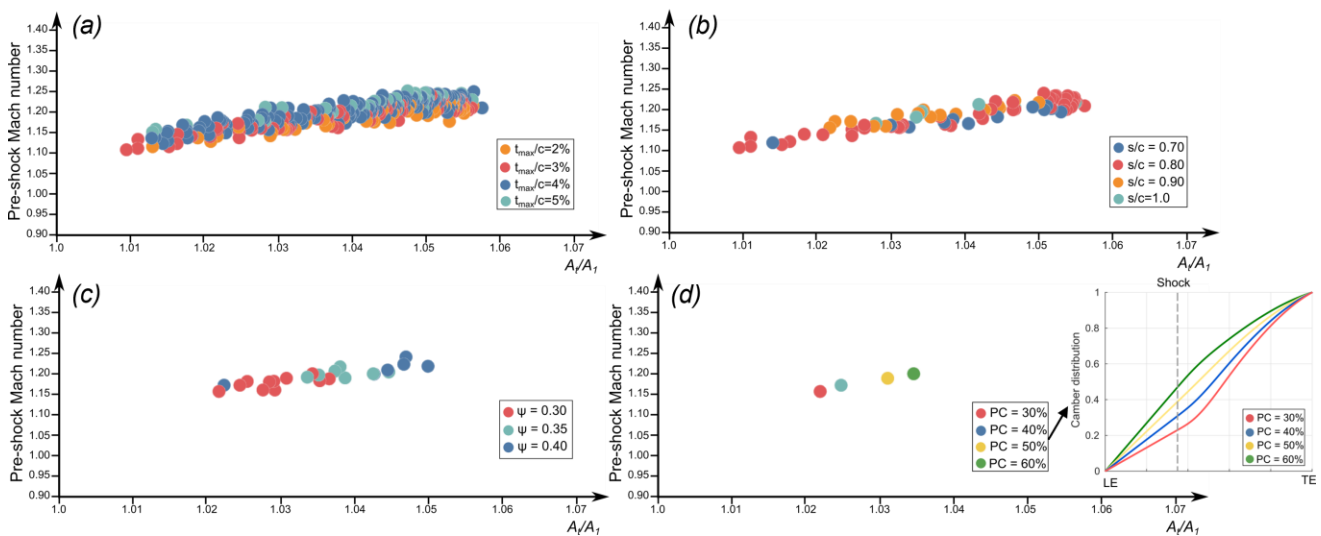


Fig. 22: Pre-shock Mach number against A_r/A_l of all designs generated and found in: <https://whittle.digital/transonic>, operating at (a) $M_{1rel} = 1.0$, (b) $M_{1rel} = 1.0$, $\alpha_{1rel} = 60^\circ$ and $t_{max}/c = 3\%$, (c) $M_{1rel} = 1.0$, $\alpha_{1rel} = 60^\circ$, $t_{max}/c = 3\%$ and $s/c=0.90$ & (d) $M_{1rel} = 1.0$, $\alpha_{1rel} = 60^\circ$, $t_{max}/c = 3\%$, $s/c=0.90$, $\psi=0.30$ and $A_{x2}/A_{x1} = 0.90$.

M_{1rel}	α_{1rel}	t_{max}/c
1.0	60°	3%
s/c	$\psi = \Delta h_o / U^2$	A_{x2}/A_{x1}
0.90	0.30	0.90

Table 3: Key geometric and aerodynamic parameters of the tip of an aerodynamically balanced front-stage rotor.

Fig. 22(a) plots all the designs, more than 700, that can be found in the database operating at a Mach number of unity. They are plotted on a pre-shock Mach number against A_t/A_1 graph. The colour coding is by t_{max}/c , ranging from 2% to 5%. In Fig. 22(b) the designs are further restricted to operate at $\alpha_{1rel} = 60^\circ$ and have a $t_{max}/c = 3\%$. 102 designs are now left which are colour coded by s/c . If s/c is further picked, in this case to be equal to 0.90, 25 blade designs can be seen to remain in Fig. 22(c). It can be seen that no $\psi=0.45$ design exists. This indicates the upper limit in the subsonic diffusion possible.

Finally, after setting $\psi=0.30$ and $A_{x2}/A_{x1} = 0.90$, which set the outlet relative Mach number triangle, only four designs are left. This is shown in Fig. 22(d), where each colour now corresponds to a given camber distribution, as shown by the enlarged inset. Each camber style is set by a percentage of overall camber up to the throat, PC , as described in Section 2 using Fig. 4. As per the design objective, the yellow $PC=50\%$ design is picked as this is closest to the desired A_t/A_1 of 1.03.

If the same process is now followed for the sections also operating at $M_{1rel} = 0.85, 0.90$ and 0.95 an initial 3D rotor blade can be generated. Fig. 23 plots in red with circles the spanwise 3D A_t/A_1 of the initial design generated using the dataset after running the 3D CFD. It should be noted that this distribution is a starting point. The most optimal target design is the aerodynamically balanced design in blue with crosses.

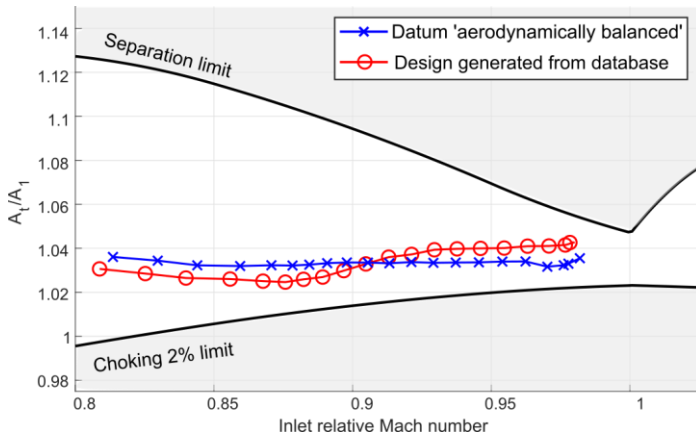


Fig. 23: Spanwise A_t/A_1 distribution from hub-to-tip, predicted using 3D CFD, of a representative transonic front stage compressor rotor generated by picking sections from the database that match the given boundary conditions across it (red with circles) compared to the target aerodynamically balanced design (blue with crosses).

The reason for the discrepancy between the two A_t/A_1 spanwise distributions is twofold. First, because the blade generated is a smooth spanwise interpolation of only four sections. Second, because the radial contraction change across the section is assumed linear in the database, as depicted in Fig. 2, when in practice this is not the case.

However, the key message from Fig. 23 is that this initial design generated easily using the database, is close enough to an

aerodynamically balanced design, making it a feasible efficient transonic rotor given the boundary conditions and early design choices made. This is because it can be redesigned to be aerodynamically balanced in 3-5 steps utilising the simple physics-based design method in [13], which accounts for the 3D radial flow changes within the blade passage during iterative design. Other boundary conditions can now be explored in the same way using the A_t/A_1 database to generate the initial 3D blade.

9. CONCLUSIONS

A web-interactive database of more than 10,000 transonic compressor and fan blade designs is used to demonstrate that over most of a civil transonic compressor and fan's operation three key transonic flow features are present: A) the shock terminates ahead of the throat plane, B) the pressure is relatively uniform by the throat plane, and C) an effectively isentropic streamtube exists within the blade passage. These three transonic flow features, A, B & C together, are what results in A_t/A_1 setting the transonic blade row's pressure rise boundaries across the shock. Based on this analysis, Fig. 10 presents the most comprehensive set of limit lines of shock-boundary layer separation and choking published up to this point, which are important for quantitatively assessing the performance of any 3D transonic compressor or fan blade.

Using this new understanding, it has been explained why the effect of a change in A_t/A_1 on the shock does not depend on how it was geometrically achieved. For example, the effect of thickening or contracting the radial streamtubes of a datum blade on the shock is similar if the resulting change in A_t/A_1 is the same. Hence, only a 1D type of assessment in A_t/A_1 is required.

In addition, it has been shown that the pre-shock Mach number of a given section, which the design objective is to minimise, is to first-order dependent on a transonic blade section's A_t/A_1 . To second order the shock is dependent on how the A_t/A_1 change was achieved with the following key variables: t_{max}/c , α_{1rel} and A_{x2}/A_{x1} shown to introduce the most scatter. After these key geometric and aerodynamic parameters have been set in the preliminary design phase, the pre-shock Mach number becomes purely a function of A_t/A_1 .

These findings suggest that at the point of the 3D design, detailed blade sectional profiling has little practical impact. Hence, the purpose of the sectional detailed design phase should be solely to make the desired changes in the real spanwise 3D A_t/A_1 . In calculating A_t/A_1 , it has been shown that the changes in 3D radial flow within the passage, which inherently occur whenever a sectional geometry change is applied, have to be taken into account. Hence, the key is to extract A_t/A_1 accurately enough in an appropriate 3D environment.

For this purpose, an assessment was made on whether low-order methods such as the throughflow are adequate or if higher fidelity 3D CFD should be brought in earlier in the design process. This is because a key aspect of multistage compressor design is providing appropriate boundary conditions for the design of an efficient transonic blade row. If the spanwise distribution of A_t/A_1 is significantly unbalanced at this early stage, it will probably be hard to fix in the 3D detailed design phase.

Overall, a key conclusion is that the throughflow is a poor lower-order design method for assessing the feasibility of efficient transonic designs, as it is too sensitive to deviation and blockage. Thus, it can even mislead the design process. In practice, even at this early design stage, 3D CFD should be used, as this enables the accurate extraction of the spanwise 3D A/A_1 . This can be done reliably by using the published A/A_1 dataset and fast 3D CFD for the initial transonic blade generation. Coupled with the simple and quick design method proposed in [13], this new early design method proposed could play a key part in the exploration and the successful development of future more efficient multistage compressors.

ACKNOWLEDGEMENTS

The author would like to thank the Royal Academy of Engineering for their financial support through their Research Fellowship. A special thanks is extended to Nick Cumpsty for his direct involvement and in instigating many of the ideas presented in this paper; as well as to my collaborators within Rolls-Royce. Finally, from the Whittle Laboratory, I would like to thank Aljaz Kotnik and Graham Pullan for their help with setting up the dbslice demos and Leo Maden and John Denton for their help in setting up the throughflow calculations. Finally, I would like to thank Mark Drela, for without his code MISES such a wide-ranging study on transonic compressors would not be possible.

NOMENCLATURE

A	3D area
bl	boundary layer
c	true chord
LE/TE	leading/trailing edge
M	Mach number
o	2D section throat passage length
P	pressure
PC	percentage of total camber up to the throat
s	pitch
t	thickness
α	flow angle measured from meridional
δ	blockage from the blade thickness
ζ_s	entropy loss coefficient= $T_2\Delta s/(h_{o1}-h_1)$
ψ	blade aerodynamic loading coefficient: $\Delta h_o/U^2$
χ	blade suction surface angle
1D/2D/3D	one/two/three-dimensional

SUBSCRIPTS

bl	including the boundary layer displacement
des	at design condition
is	isentropic
rel	relative frame
sh	shock foot
t	evaluated at the throat plane
x	axial plane
1/2	evaluated at the inlet/outlet plane

REFERENCES

- [1] S. Lieblein and I. A. Johnsen, "Resume of Transonic Compressor Research at NACA Lewis Laboratory," *ASME J. of Eng. Power*, vol. 83, no. 3, pp. 219-232, 1961.
- [2] H. Starcken, "Loss Development in Transonic Compressor Cascades," *von Karman Institute for Fluid Dynamics Lecture Series, Transonic Compressors, Feb 1-5, 1988*, 1988.
- [3] H. Schreiber, "Shock Losses in Transonic and Supersonic Compressor Cascades," *von Karman Institute for Fluid Dynamics Lecture Series, Transonic Compressors, Feb 1-5, 1988*, 1988.
- [4] J. L. Kerrebrock, "Flow in Transonic Compressors," *AIAA Journal*, vol. 19, no. 1, pp. 1-11, 1981.
- [5] P. E. Wright and D. C. Miller, "An Improved Compressor Performance Prediction Model," in *IMEchE European Conference, 19-20 March 1991, Turbomachinery - Latest development in a changing scene, Paper No. C423/028*, 1981.
- [6] L. H. Smith, "Axial Compressor Aerodesign Evolution at General Electric," *ASME J. of Turbomachinery*, vol. 124, no. 3, pp. 321-330, 2002.
- [7] A. R. Wadia and W. W. Copenhaver, "An Investigation of the Effect of Cascade Area Ratios on Transonic Compressor Performance," *ASME J. of Turbomachinery*, vol. 118, no. 4, pp. 760-770, 1996.
- [8] C. Freeman and N. A. Cumpsty, "Method for the prediction of supersonic compressor blade performance," *AIAA J. of Propulsion*, vol. 8, no. 1, 1992.
- [9] J. H. Page, P. Hield and P. G. Tucker, "Inverse Design of 3D Multistage Transonic Fans at Dual Operating Points," *ASME J. of Turbomachinery*, vol. 136, no. 4, pp. 1-9, 2014.
- [10] H. Okui, R. A. Verstraete, R. A. Van den Braembussche and Z. Alsalihi, "Three-Dimensional Design and Optimization of a Transonic Rotor in Axial Flow Compressors," *ASME J. of Turbomachinery*, vol. 135, no. 3, pp. 1-11, 2013.
- [11] P. Seshadri, S. Shahpar, P. Constantine, G. Parks and M. Adams, "Turbomachinery Active Subspace Performance Maps," *ASME J. of Turbomachinery*, vol. 140, no. 4, pp. 1-11, 2018.
- [12] D. Lefas and R. J. Miller, "Transonic Relief in Fans and Compressors," *ASME J. of Turbomachinery*, vol. 144, no. 5, pp. 1-14, 2022.
- [13] D. Lefas and R. J. Miller, "Design of Aerodynamically Balanced Transonic Compressor Rotors," *ASME J. of Turbomachinery*, vol. 146, no. 2, pp. 1-14, February 2024.
- [14] G. Pullan, "A Web-Based Database Approach to CFD Post-Processing," in *55th AIAA Aerospace Sciences Meeting, Grapevine, Texas, 2017*.
- [15] G. Pullan, "Making use of our data," *J. Glob. Power Propuls. Soc.*, no. Special Issue: Data-driven modelling and high-fidelity simulations, pp. 1-13, 2021.

- [16] B. M. Kulfan, "Universal Parametric Geometry Representation Method," *AIAA Journal of Aircraft*, vol. 45, no. 1, pp. 142 - 158, 2008.
- [17] M. N. Goodhand, R. J. Miller and H. W. Lung, "The Impact of Geometric Variation on Compressor Two-Dimensional Incidence Range," *ASME J. of Turbomachinery*, vol. 137, no. 2, pp. 1-7, 2015.
- [18] M. Drela and H. Youngren, "A User's Guide to MISES 2.53," Massachusetts Institute of Technology, Cambridge, MA, 1998.
- [19] M. Drela and M. B. Giles, "Viscous-Inviscid Analysis of Transonic Low Reynolds Number Aerofoils," *AIAA Journal*, vol. 25, no. 10, 1987.
- [20] H. Youngren and M. Drela, "Viscous/Inviscid Method for the Preliminary Design of Transonic Cascades," in *27th Joint Propulsion Conference*, Sacramento, CA, U.S.A, June, 1991.
- [21] B. Kusters, H. A. Schreiber, U. Koller and R. Monig, "Development of Advanced Compressor Airfoils for Heavy Duty Gas Turbines—Part II: Experimental and Analytical Analysis," *ASME J. of Turbomachinery*, vol. 122, no. 3, pp. 406-414, 1999.
- [22] T. Brandvik and G. P. Pullan, "An Accelerated 3D Navier Stokes Solver for Flows in Turbomachines," *ASME J. of Turbomachinery*, vol. 133, no. 2, pp. 1-9, 2010.
- [23] P. Spalart and S. Almaras, "A One Equation Turbulence Model for Aerodynamic Flows," *AIAA Journal*, Vols. 94-439, no. 1, pp. 5-21, 1992.
- [24] J. Denton, "Throughflow Calculations for Transonic Axial Flow Turbines," *ASME J. of Turbomachinery*, vol. 100, pp. 212-218, 1978.